J. Iron Steel Res. Int.
https://doi.org/10.1007/s42243-024-01225-2

ORIGINAL PAPER

Phase equilibria of Fe_3O_4–Cr_2O_3–CaO system: experimental measurements and thermodynamic calculations

Ao Zhu[1] · **Chen-ying Shi**[2] · **Pei-yuan Ni**[3] · **Teng-fei Deng**[1]

Received: 28 November 2023 / Revised: 5 January 2024 / Accepted: 9 January 2024

Abstract

Understanding the phase equilibria of the Fe_3O_4–Cr_2O_3–CaO system is essential for the efficient recycling of stainless steel pickling sludge. The isothermal section of this system at 1473 K under oxygen partial pressure of 0.15 Pa was investigated. Key experiments on the relevant binary systems were conducted using a combination of equilibrium-quenching techniques, X-ray diffraction, high-resolution transmission electron microscope, and electron probe microanalysis. These systems were rigorously assessed using the CALPHAD (CALculation of Phase Diagram) method, incorporating the present experimental data. The liquid phase was modeled using the ionic two-sublattice model, represented as $(Ca^{2+}, Cr^{3+}, Fe^{2+})_P(O^{2-}, Va, FeO_{1.5})_Q$, where Va represents vacancy, and P and Q denote the number of sites on the cation and anion sublattices, respectively. To ensure electroneutrality, the values of P and Q adjust according to the composition of the mixture. From this, the isothermal section of the Fe_3O_4–Cr_2O_3–CaO system at 1473 K under the specified oxygen partial pressure was obtained based on the thermodynamic parameters of the binary systems. The present experimental data and calculation results hold significant implications for the comprehensive recycling of stainless steel pickling sludge.

Keywords Fe_3O_4–Cr_2O_3–CaO system · Ionic two-sublattice model · Phase equilibria · CALPHAD

1 Introduction

Stainless steel, a critical material in the modern steel industry, is widely used due to its extensive application potential. During its production, acids like H_2SO_4, HNO_3, and HF are employed for surface pickling, enhancing its corrosion resistance and appearance [1, 2]. This process generates pickling wastewater, typically treated through neutralization and sedimentation, leading to the generation of stainless steel pickling sludge (SSPS). SSPS, containing valuable metals like iron and chromium, is categorized as hazardous solid waste due to its high concentration of heavy metals (HMs) and fluorine [3, 4]. Chromium, a costly and vital raw material in metallurgical and chemical industries [5], is a key focus in SSPS recovery research. The SSPS mainly contains FeO_n, Cr_2O_3, and calcium containing compounds. If FeO_n and Cr_2O_3 can be reorganized into spinel phase and separated, high-value chromite can be obtained from the sludge. Understanding the phase equilibrium relationship of the FeO_n–Cr_2O_3–CaO system and identifying the chromite phase region are crucial for efficient utilization of SSPS resources. To enhance the efficiency of obtaining phase equilibrium information, thermodynamic calculations using appropriate databases and software are recommended. Using CALPHAD (CALculation of PHAse Diagram) method, in particular, can provide a self-consistent database. When combined with suitable software, this method can significantly reduce costs and time in material development, offering effective guidance for material design [6].

Currently, the ternary phase diagram of the FeO_n–Cr_2O_3–CaO system remains undocumented, highlighting

---

✉ Teng-fei Deng
dengtf@whut.edu.cn

Pei-yuan Ni
nipeiyuan@smm.neu.edu.cn

[1] State Key Laboratory of Silicate Materials for Architectures, Wuhan University of Technology, Wuhan 430070, Hubei, China

[2] College of Chemistry and Chemical Engineering, Central South University, Changsha 410083, Hunan, China

[3] Key Laboratory of Ecological Metallurgy of Multi-Metal Intergrown Ores of Education Ministry, School of Metallurgy, Northeastern University, Shenyang 110819, Liaoning, China

the importance of investigating its phase equilibrium. Previous studies have reported phase diagrams [7–14] and thermodynamic evaluations [15–18] for related binary systems. Taylor and Dinsdale [15] focused on the Fe–Cr–O system, adopting the ionic two-sublattice model to represent the liquid phase as $(Fe^{2+}, Fe^{3+}, Cr^{3+})_P(O^{2-}, Va)_Q$, where Va represents vacancy, and P and Q denote the number of sites on the cation and anion sublattices, respectively. To ensure electroneutrality, the values of P and Q adjust according to the composition of the mixture. In contrast, Kjellqvist et al. [16] deviated from this approach in their evaluation of liquid Fe_2O_3. They introduced $FeO_{1.5}$ as a neutral molecule on the anion sublattice, rather than using separate cation and anion sublattices. This modification arose due to complications in more complex systems. Selleby and Sundman [17] evaluated the Fe–Ca–O system, also using the ionic two-sublattice model for the liquid phase. Meanwhile, Degterov and Pelton [18] focused on the CaO–CrO_n system, employing a modified quasi-chemical model for the liquid phase. However, their study was confined to conditions of low oxygen partial pressure. The ionic two-sublattice model, which has been used to describe both oxide and metallic liquids in various studies [19, 20], is adopted in the current work. This model offers a versatile framework for parameterizing these complex systems, facilitating a deeper understanding of the FeO_n–Cr_2O_3–CaO system.

The primary objective of this study is to perform crucial experiments on the binary systems within the Fe_3O_4–Cr_2O_3–CaO system. Following these experiments, the isothermal section of the Fe_3O_4–Cr_2O_3–CaO system at 1473 K under oxygen partial pressure of 0.15 Pa will be determined using the CALPHAD method.

2 Experimental

2.1 Sample preparation

This study aims to investigate the phase equilibrium relationship of the Fe_3O_4–Cr_2O_3–CaO system at 1473 K. To achieve this, we conducted experiments on the binary systems of Fe_3O_4–Cr_2O_3, Fe_3O_4–CaO and CaO–Cr_2O_3. The starting materials were Fe_3O_4 powder (99.99 wt.% purity, Sigma-Aldrich, USA), Cr_2O_3 powder (99.97 wt.% purity, Alfa Aesar, USA) and CaO powder (99.99 wt.% purity, Sinopharm Chemical Reagent Co., Ltd., China). These powders were proportionally mixed and ground using an agate mortar for 30 min to ensure homogeneity. The composition of the samples is detailed in Table 1. Approximately 1 g of this mixture was then compressed into a cylinder with diameter of 10 mm at a uniaxial pressure of 10 MPa and placed in a nickel crucible. During the heating process, the nickel crucible with the sample, secured with nickel wire, was suspended in a tube furnace (Henan Nobody Materials Science and Technology Co., Ltd., China) and heated by a $MoSi_2$ heating element. Temperature control was achieved using an S-type thermocouple, maintaining accuracy within ± 5 K. The samples were equilibrated at the target temperature for 48 h under a 99.999% pure argon atmosphere, which maintained the oxygen partial pressure at 0.15 Pa. After equilibration, the samples, still in their nickel crucibles, were rapidly quenched in quenching oil. For further analysis, these quenched samples were embedded in epoxy resin and polished.

Table 1 Initial composition of samples (wt.%)

Sample	Fe_3O_4	Cr_2O_3	CaO
1	5.5	94.5	
2	10.5	89.5	
3	34.9	65.1	
4	38.9	61.1	
5	60.0	40.0	
6	63.0		37.0
7	90.0		10.0
8	85.0		15.0
9		80.0	20.0
10		60.0	40.0

2.2 Sample characterization

Phase identification in this study was conducted using an X-ray diffractometer (XRD, D8-Advanced, Bruker, Germany) equipped with Cu Kα radiation at 40 kV and 40 mA. Scans spanned a 2θ range from 10° to 80°, with a step size of 0.02°. Additionally, the microstructures of the samples in the Fe_3O_4–Cr_2O_3 system were examined using a high-resolution transmission electron microscope (HRTEM, Tecnai G2 F20 S-Twin, FEI, America). The solid solubility of the system was determined using an energy-dispersive X-ray spectrometer (EDS). To identify the eutectic reaction temperature in the Fe_3O_4–CaO system, a simultaneous thermal analyzer (STA449F3, Netzsch, Germany) was employed, with a heating rate of 5 K/min and argon as the carrier gas. Further characterization of the microstructures in the Fe_3O_4–CaO system was performed using a scanning electron microscope (SEM), complemented by electron probe microanalysis (EPMA, EPMA–1720T, Shimadzu, Japan). EPMA analyses were conducted at 15 kV and 2×10^{-8} A. For precise phase composition and elemental measurement, pure Fe_2O_3

(99.99 wt.%) and $CaCO_3$ (99.99 wt.%) were used as standard materials in the wavelength-dispersive X-ray spectrometer (WDS).

3 Thermodynamic models

In this study, the CALPHAD method [21] was employed to compute the phase diagram of the Fe_3O_4–Cr_2O_3–CaO system. For the thermodynamic assessment, the Thermo-Calc software package [22] was utilized. The thermodynamic models for all stable phases present in the Fe_3O_4–Cr_2O_3–CaO system are comprehensively outlined in Table 2.

3.1 Liquid phase

The liquid phase in this study is characterized using the ionic two-sublattice model, represented by the formula $(Ca^{2+}, Cr^{3+}, Fe^{2+})_P(O^{2-}, Va, FeO_{1.5})_Q$. The Gibbs energy of the liquid phase G_m^{Liquid} is expressed as follows:

$$\begin{aligned} G_m^{Liquid} = {} & y_{Ca^{2+}} y_{O^{2-}} {}^0G^{Liquid}_{Ca^{2+}:O^{2-}} + y_{Cr^{3+}} y_{O^{2-}} {}^0G^{Liquid}_{Cr^{3+}:O^{2-}} + \\ & y_{Fe^{2+}} y_{O^{2-}} {}^0G^{Liquid}_{Fe^{2+}:O^{2-}} + \\ & Q\left(y_{Ca^{2+}} y_{Va} {}^0G^{Liquid}_{Ca} + y_{Cr^{3+}} y_{Va} {}^0G^{Liquid}_{Cr} + y_{Fe^{2+}} y_{Va} {}^0G^{Liquid}_{Fe} + y_{FeO_{1.5}} {}^0G^{Liquid}_{FeO_{1.5}}\right) + \\ & PRT\left(y_{Ca^{2+}} \ln y_{Ca^{2+}} + y_{Cr^{3+}} \ln y_{Cr^{3+}} + y_{Fe^{2+}} \ln y_{Fe^{2+}}\right) + \\ & QRT\left(y_{O^{2-}} \ln y_{O^{2-}} + y_{Va} \ln y_{Va} + y_{FeO_{1.5}} \ln y_{FeO_{1.5}}\right) + {}^EG_m^{Liquid} \end{aligned} \tag{1}$$

where y represents the site fraction; R is the universal gas constant; T is temperature, K; and ${}^0G_i^{Liquid}$ is the molar Gibbs energy of the end member in the model. The expression for ${}^EG_m^{Liquid}$ is given by the following equation, including only the parameters that have been used.

$$\begin{aligned} {}^EG_m^{Liquid} = {} & y_{Cr^{3+}} y_{Fe^{2+}} y_{O^{2-}} L^{Liquid}_{Cr^{3+},Fe^{2+}:O^{2-}} + y_{Cr^{3+}} y_{Fe^{2+}} y_{Va} L^{Liquid}_{Cr^{3+},Fe^{2+}:Va} \\ & + y_{Cr^{3+}} y_{O^{2-}} y_{Va} L^{Liquid}_{Cr^{3+}:O^{2-},Va} + y_{Fe^{2+}} y_{O^{2-}} y_{Va} L^{Liquid}_{Fe^{2+}:O^{2-},Va} \\ & + y_{Fe^{2+}} y_{O^{2-}} y_{FeO_{1.5}} L^{Liquid}_{Fe^{2+}:O^{2-},FeO_{1.5}} + y_{Cr^{3+}} y_{O^{2-}} y_{FeO_{1.5}} L^{Liquid}_{Cr^{3+}:O^{2-},FeO_{1.5}} \\ & + y_{Fe^{2+}} y_{FeO_{1.5}} y_{Va} L^{Liquid}_{Fe^{2+}:FeO_{1.5},Va} + y_{Cr^{3+}} y_{Fe^{2+}} y_{O^{2-}} y_{Va} L^{Liquid}_{Cr^{3+},Fe^{2+}:O^{2-},Va} \\ & + y_{Ca^{2+}} y_{Fe^{2+}} y_{O^{2-}} L^{Liquid}_{Ca^{2+},Fe^{2+}:O^{2-}} + y_{Ca^{2+}} y_{Fe^{2+}} y_{O^{2-}} y_{FeO_{1.5}} L^{Liquid}_{Ca^{2+},Fe^{2+}:O^{2-},FeO_{1.5}} \\ & + y_{Ca^{2+}} y_{O^{2-}} y_{FeO_{1.5}} L^{Liquid}_{Ca^{2+}:O^{2-},FeO_{1.5}} + y_{Ca^{2+}} y_{O^{2-}} y_{Va} L^{Liquid}_{Ca^{2+}:O^{2-},Va} \\ & + y_{Ca^{2+}} y_{Fe^{2+}} y_{Va} L^{Liquid}_{Ca^{2+},Fe^{2+}:Va} + y_{Ca^{2+}} y_{Va} y_{FeO_{1.5}} L^{Liquid}_{Ca^{2+}:Va,FeO_{1.5}} \\ & + y_{Ca^{2+}} y_{Cr^{3+}} y_{O^{2-}} L^{Liquid}_{Ca^{2+},Cr^{3+}:O^{2-}} \end{aligned} \tag{2}$$

where L signifies the interaction parameter, which is designed to vary linearly with temperature. The initial fourteen interaction parameters are derived from binary subsystems, as referenced in previous studies [16, 17, 23]. The final interaction parameter has been specifically evaluated in this work.

Table 2 Thermodynamic models of all stable phases in Fe_3O_4–Cr_2O_3–CaO system in present work

Phase	Model	Source
Liquid	$(Ca^{2+}, Cr^{3+}, Fe^{2+})_P(O^{2-}, Va, FeO_{1.5})_Q$	This work
CF ($CaO{\cdot}Fe_2O_3$)	$(Ca^{2+})_1(Fe^{3+})_2(O^{2-})_4$	Ref. [17]
C_2F ($2CaO{\cdot}Fe_2O_3$)	$(Ca^{2+})_2(Fe^{3+})_2(O^{2-})_5$	Ref. [17]
CF_2 ($CaO{\cdot}2Fe_2O_3$)	$(Ca^{2+})_1(Fe^{3+})_4(O^{2-})_7$	Ref. [17]
Halite (wüstite, lime)	$(Ca^{2+}, Cr^{3+}, Fe^{2+}, Fe^{3+}, Va)_1(O^{2-})_1$	This work
Spinel (magnetite, chromite)	$(Cr^{2+}, Cr^{3+}, Fe^{2+}, Fe^{3+})_1(Ca^{2+}, Cr^{3+}, Fe^{2+}, Fe^{3+}, Va)_2(Fe^{2+}, Va)_2(O^{2-})_4$	This work
Corundum (hematite, eskolaite)	$(Cr^{2+}, Cr^{3+}, Fe^{3+})_2(Cr^{3+}, Va)_1(O^{2-})_3$	Ref. [15]
α-$CaCr_2O_4$, β-$CaCr_2O_4$	$(Ca^{2+})_1(Cr^{3+})_2(O^{2-})_4$	This work

3.2 CF and C_2F phases

The molar Gibbs energy for the CF and C_2F phases is characterized using the following descriptions:

$$ {}^0G - H_i^{SER} = a + bT + cT\ln T + dT^{-1} + eT^2 \tag{3}$$

where ${}^0G$ represents the molar Gibbs energy of CF or C_2F; H_i^{SER} represents the enthalpy of element i at the standard state of 298.15 K and 10^5 Pa, as well as the reference state relative to the stable element reference (SER); and a, b, c, d, and e are coefficients. The thermodynamic parameters of CF and C_2F previously reported in Ref. [17] are deemed reliable and have thus been adopted in the present study.

3.3 Halite, spinel and corundum phases

The halite, spinel and corundum phases in this study are modeled using the compound energy formalism (CEF) [23]. Specifically, in the halite phase model, it is assumed that two Fe^{3+} ions can replace three Fe^{2+} ions on the cation sublattice. This substitution results in the formation of neutral vacancies on the cation sublattice to maintain a balance of sites. Additionally, it is presumed that Ca^{2+} and Cr^{3+} can substitute the cation sublattice as well. Therefore, the halite phase is formulated as $(Ca^{2+}, Cr^{3+}, Fe^{2+}, Fe^{3+}, Va)_1(O^{2-})_1$.

Based on the evaluation of the Fe–O system [24], the spinel phase is modeled using a four-sublattice approach. This model designates two sublattices for typical tetrahedral and octahedral cation sites, one for oxygen anions and the other to accommodate Fe^{2+} ions at the normally cation-free octahedral sites. In this framework, Ca is assumed to only enter the second sublattice, while Cr can enter both the first and second sublattices. The spinel phase is thus described by the CEF as $(Cr^{2+}, Cr^{3+}, Fe^{2+}, Fe^{3+})_1(Ca^{2+}, Cr^{3+}, Fe^{2+}, Fe^{3+}, Va)_2(Fe^{2+}, Va)_2(O^{2-})_4$.

The corundum phase in this study is modeled as a solid solution, representing a complete miscibility between stoichiometric Fe_2O_3 and Cr_2O_3 across all temperatures. Accordingly, the corundum phase is formulated as $(Cr^{2+}, Cr^{3+}, Fe^{3+})_2(Cr^{3+}, Va)_1(O^{2-})_3$. This model reflects the interchangeable nature of the oxides within the corundum structure.

3.4 α-$CaCr_2O_4$, β-$CaCr_2O_4$ and CF_2 phases

The low-temperature form of β-$CaCr_2O_4$ exhibits a spinel structure [25], while the high-temperature counterpart, α-$CaCr_2O_4$, shares the same structural characteristics as $SrCr_2O_4$ [26]. Both α-$CaCr_2O_4$ and β-$CaCr_2O_4$, along with the CF_2 phase, are stoichiometric compounds. Their Gibbs energies can be described in terms of the corresponding pure oxide and its deviations, under the assumption that the Neumann–Kopp rule is applicable to the heat capacity. The expression for their Gibbs energies is formulated as follows:

$$^{0}G_{\mathrm{m}}^{\mathrm{CaCr_2O_4}} = {}^{0}G_{\mathrm{CaO}} + {}^{0}G_{\mathrm{Cr_2O_3}} + a + bT \tag{4}$$

$$^{0}G_{\mathrm{m}}^{\mathrm{CF_2}} = {}^{0}G_{\mathrm{CaO}} + 2\,{}^{0}G_{\mathrm{Fe_2O_3}} + a + bT \tag{5}$$

4 Results

4.1 Phase equilibria of Fe_3O_4–Cr_2O_3 system under oxygen partial pressure of 0.15 Pa at 1473 K

The phase equilibrium relations of five distinct component samples in the Fe_3O_4–Cr_2O_3 system were examined. Initial characterization of the crystal phases in the quenched samples was conducted through XRD measurements. To provide deeper insights into the microstructure and composition of each crystal phase, HRTEM and EDS were employed. Figure 1 displays the XRD patterns of five quenched samples at 1473 K in the Fe_3O_4–Cr_2O_3 system. Analysis of these patterns reveals the presence of two crystal phases at 1473 K: Cr_2O_3 (ICDD No. 00-038-1479) and $FeCr_2O_4$ (ICDD No. 01–089-2618). In quenched Samples 1 and 2, both Cr_2O_3 and $FeCr_2O_4$ phases were identified, suggesting that the compositions of these samples fall within the two-phase region of Cr_2O_3 and $FeCr_2O_4$. In contrast, only the $FeCr_2O_4$ phase was observed in quenched Samples 3–5, indicating complete dissolution of Cr_2O_3 into Fe_3O_4, resulting in the formation of $FeCr_2O_4$.

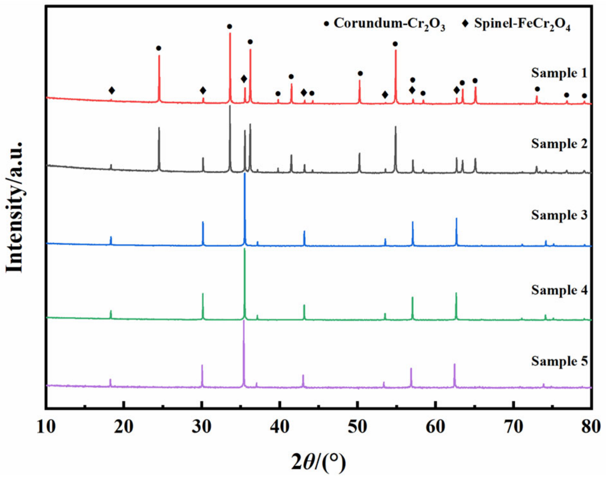

Fig. 1 XRD patterns of five quenched samples at 1473 K in Fe_3O_4–Cr_2O_3 system

HRTEM and EDS were utilized to delve into the microstructure and composition of two crystal phases. Figure 2 presents the transmission electron microscopy (TEM) images of quenched Sample 2. Specifically, Fig. 2a displays the TEM image of $FeCr_2O_4$, while Fig. 2b reveals the HRTEM image taken from Fig. 2a. In this image, an interplanar spacing d of 0.259 nm is evident, aligning with the $(3\bar{1}\bar{1})$ crystal plane of $FeCr_2O_4$. $FeCr_2O_4$ is characterized by a spinel structure within the cubic crystal system and is classified under the space group $Fd\bar{3}m$. The selected area electron diffraction (SAED) pattern in Fig. 2c showcases the diffraction spots of the $(11\bar{1})$, $(3\bar{1}\bar{1})$ and $(1\bar{3}1)$ planes along the [112] direction. Turning to Cr_2O_3, Fig. 2d exhibits the TEM image, with an interplanar spacing of 0.281 nm highlighted in Fig. 2e, corresponding to the $(0\bar{1}4)$ crystal plane of Cr_2O_3. Cr_2O_3 possesses a corundum structure and falls within the rhombohedral crystal system, under the space group $R\bar{3}c$. The SAED pattern in Fig. 2f, related to the image in Fig. 2e, displays the diffraction spots of the $(\bar{2}1\bar{3})$, $(\bar{2}01)$ and $(0\bar{1}4)$ planes along the [182] direction. A comparison with the standard PDF card (ICDD No. 00-038-1479) reveals a slight increase in the interplanar spacing of the $(0\bar{1}4)$ crystal plane of Cr_2O_3, potentially attributed to Fe^{3+} incorporation into Cr_2O_3. The compositional details of these phases are provided in Table 3. In conclusion, at 1473 K, the Fe_3O_4–Cr_2O_3 system exhibits three-phase equilibrium relationships: a two-phase equilibrium between $FeCr_2O_4$ and Cr_2O_3, a singular $FeCr_2O_4$ phase, and a singular Cr_2O_3 phase.

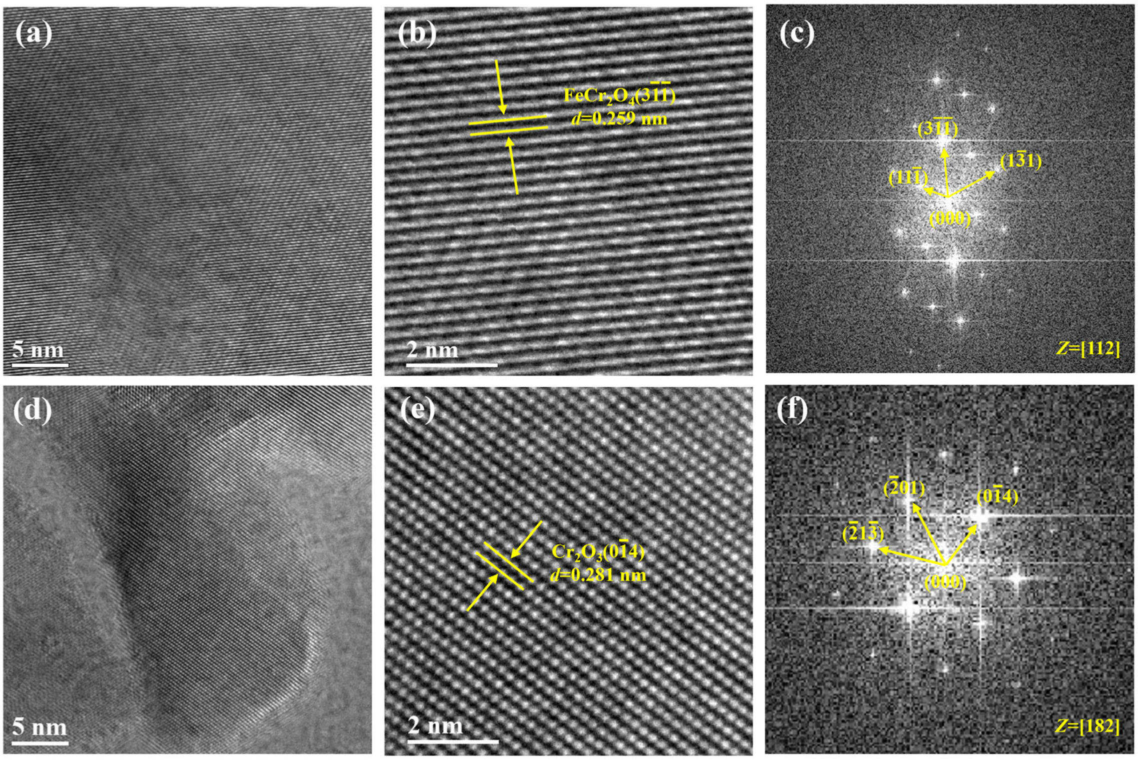

Fig. 2 TEM pattern of quenched Sample 2. **a** TEM image of $FeCr_2O_4$; **b** HRTEM image of $FeCr_2O_4$; **c** SAED pattern corresponding to **b**; **d** TEM image of Cr_2O_3; **e** HRTEM image of Cr_2O_3; **f** SAED pattern corresponding to **e**

Table 3 Composition of corresponding phases in Fe_3O_4–Cr_2O_3 system (wt.%)

Phase	Fe_3O_4	Cr_2O_3
$FeCr_2O_4$	37.2	62.8
Cr_2O_3	3.2	96.8

4.2 Eutectic reaction of Fe_3O_4–CaO system under oxygen partial pressure of 0.15 Pa

Based on the thermodynamic parameters assessed by Selleby and Sundman [17], a eutectic reaction in the Fe_3O_4–CaO system was identified under oxygen partial pressure of 0.15 Pa, with the calculated eutectic reaction temperature being 1475 K. To validate these calculated results, experimental studies on the eutectic reaction were conducted. The eutectic temperature was initially determined using differential scanning calorimetry (DSC) in a simultaneous thermal analyzer. The DSC curve of Sample 8 is depicted in Fig. 3. This curve, which extends from 800 to 1600 K, is shown as a solid line, with a dashed line indicating the enlarged section of the curve. Generally, the DSC curve tends downward, indicating that the specific heat of the sample does not vary significantly with temperature. Notably, an endothermic peak is observed on the DSC curve, which corresponds to the eutectic reaction of Liquid → $Ca_2Fe_2O_5 + Fe_3O_4$. The onset temperature of the eutectic reaction, based on the DSC curve, is determined to be 1485 K. However, considering the potential lag caused by the heating rate during detection, the calculated eutectic temperature of 1475 K is deemed reasonable. This consideration helps align the experimental observations with the thermodynamic calculations.

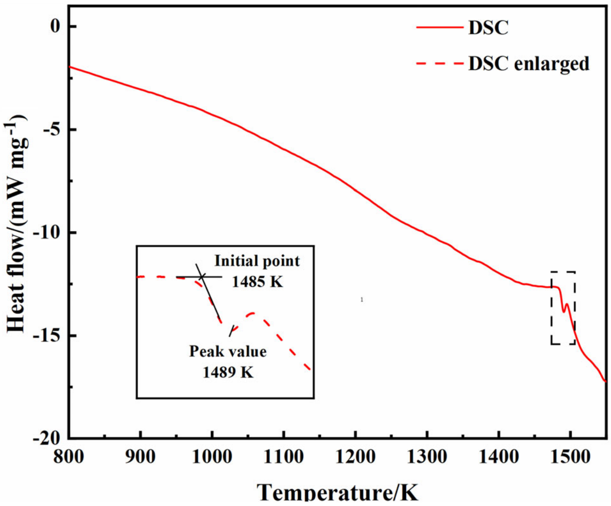

Fig. 3 DSC curve of Sample 8 in heat flow–temperature graph. Solid line means DSC curve from 800 to 1600 K and dashed line means locally enlarged area

Quenched Sample 6 was examined to study the liquid phase composition. Figure 4 illustrates the XRD patterns of the quenched Sample 6 at 1485 K, along with the backscattered electron (BSE) micrograph. In Fig. 4a, the XRD patterns indicate the presence of $Ca_2Fe_2O_5$. As depicted in Fig. 4b, two distinct phases are observed in quenched Sample 6. The brighter phase is identified as the liquid phase, while the darker phase is recognized as $Ca_2Fe_2O_5$. Additionally, black and gray areas in the image represent pores and carbon, respectively. The liquid phase composition measured using the WDS was 81.9 wt.% Fe_3O_4. Quenched Sample 7 was used to investigate the maximum solid solubility of CaO in Fe_3O_4. The XRD patterns and BSE micrograph for quenched Sample 7 are presented in Fig. 5. The XRD patterns reveal the presence of a spinel phase in Fig. 5a. Based on Fig. 5b, both spinel and liquid phases are identified in quenched Sample 7. The maximum solid solubility of CaO in Fe_3O_4 measured using the WDS was 2.9 wt.%.

4.3 Phase equilibria of β-$CaCr_2O_4$ under oxygen partial pressure of 0.15 Pa at 1473 K

The phase diagram of the CaO–Cr_2O_3 system is significantly influenced by the oxygen partial pressure. Under reducing conditions, only $CaCr_2O_4$, which contains chromium in the (+ 3) valence state, forms in the CaO–Cr_2O_3 system. $CaCr_2O_4$ crystals are classified into high-temperature (α), low-temperature (β), and metastable (δ) forms [11, 27, 28]. Kaiser et al. [11] reported the transformation of δ-$CaCr_2O_4$ to β-$CaCr_2O_4$ at 1516 K under reducing conditions. Quenched Samples 9 and 10 were analyzed to investigate the phase equilibrium relationship of the CaO–Cr_2O_3 system at 1473 K. The XRD patterns of these samples, presented in Fig. 6, show Cr_2O_3 and β-$CaCr_2O_4$ in quenched Sample 9 and CaO and β-$CaCr_2O_4$ in quenched Sample 10. The experimental results suggest that the crystal form of $CaCr_2O_4$ at 1473 K is the low-temperature (β) form, identified using the ICDD No. 01-070-2387. The solid solubility of Cr_2O_3 in CaO decreases rapidly with temperature and is considered very small at 1473 K, making accurate measurement challenging. Consequently, the solid solubility of Cr_2O_3 in CaO at 1473 K has not been comprehensively explored in this work. Parameters reflecting this solid solubility will be addressed in the subsequent optimization process.

4.4 Thermodynamic calculations

Utilizing the CALPHAD method, thermodynamic evaluations of the Fe_3O_4–Cr_2O_3, Fe_3O_4–CaO, and Cr_2O_3–CaO systems were conducted using the PARROT module in Thermo-Calc software. This approach operates by minimizing the sum of the squared differences between experimental data and calculated results. The optimized parameters assessed in the present work are presented in Table 4. *G*CAOSOL and *G*CR2O3 are Gibbs energy expression abbreviations for solid phase CaO and Cr_2O_3, respectively, as detailed in supplementary materials. In supplementary materials, all parameters for the system are listed together with the models used.

The phase diagram of the Fe_3O_4–Cr_2O_3 system was calculated using the thermodynamic parameters provided by Kjellqvist et al. [16], with the oxygen partial pressure set at 0.15 Pa. According to the calculations of Kjellqvist et al. [16], the solid solubility of Cr_2O_3 in Fe_3O_4 is 62.3 wt.% at 1473 K, aligning with the experimental data of this study. However, there is a discrepancy in the solid solubility of Fe_3O_4 in Cr_2O_3 at 1473 K; the experimental results indicate a solubility of 3.2 wt.%, which does not match the value of 9.2 wt.% calculated by Kjellqvist et al. [16]. To reconcile the experimental data with the calculated

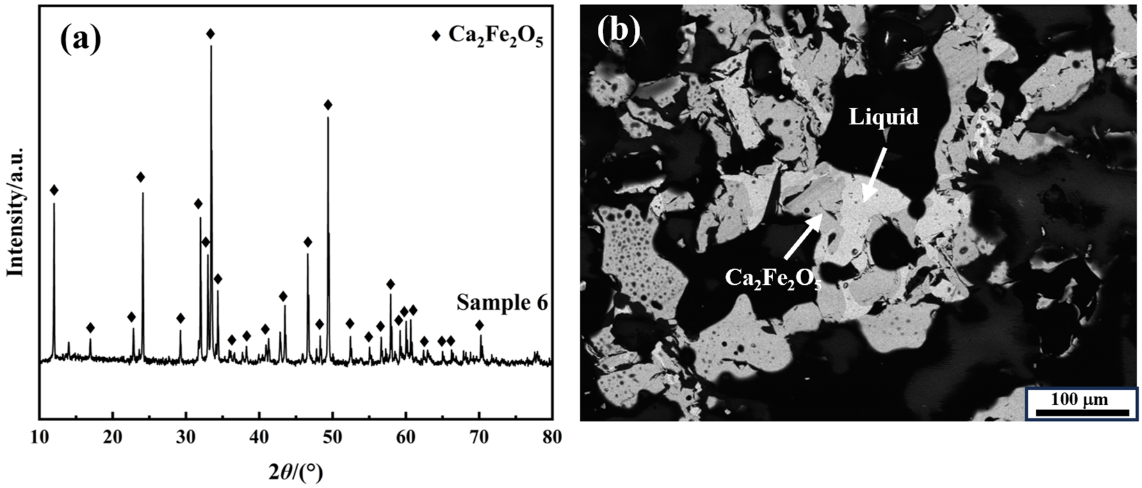

Fig. 4 XRD patterns (**a**) and backscattered electron micrograph (**b**) of quenched Sample 6

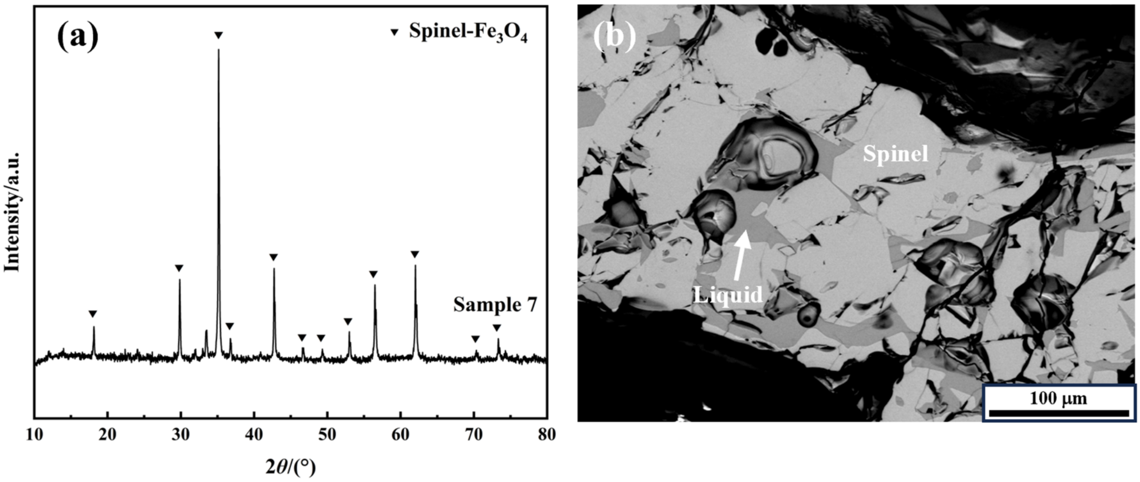

Fig. 5 XRD patterns (**a**) and backscattered electron micrograph (**b**) of quenched Sample 7

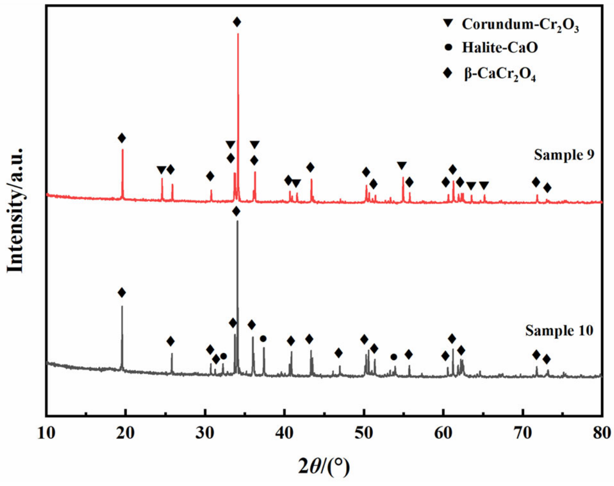

Fig. 6 XRD patterns of quenched samples at 1473 K in CaO–Cr_2O_3 system

Table 4 Thermodynamic parameters assessed in present work

Phase/Model/Parameter
Fe_3O_4–Cr_2O_3 system
Corundum (hematite, eskolaite): $(Cr^{2+}, Cr^{3+}, Fe^{3+})_2(Cr^{3+}, Va)_1(O^{2-})_3$
$^0L^{Corundum}_{Cr^{3+},Fe^{3+}:Va:O^{2-}} = -10{,}000 + 23.5T$
Cr_2O_3–CaO system
Liquid: $(Ca^{2+}, Cr^{3+})_P(O^{2-}, Va)_Q$
$L^{Liquid}_{Ca^{2+},Cr^{3+}:O^{2-}} = -181{,}326 + 25.45T$
Halite (wüstite, lime): $(Ca^{2+}, Cr^{3+}, Va)_1(O^{2-})_1$
$^0L^{Halite}_{Ca^{2+},Cr^{3+}:O^{2-}} = +55{,}000$
β-$CaCr_2O_4$: $(Ca^{2+})_1(Cr^{3+})_2(O^{2-})_4$
$^0G^{\beta-CaCr_2O_4}_{Ca^{2+}:Cr^{3+}:O^{2-}} = GCAOSOL + GCR2O3 - 59{,}922 + 3.8T$
α-$CaCr_2O_4$: $(Ca^{2+})_1(Cr^{3+})_2(O^{2-})_4$
$^0G^{\alpha-CaCr_2O_4}_{Ca^{2+}:Cr^{3+}:O^{2-}} = {}^0G^{\beta-CaCr_2O_4}_{Ca^{2+}:Cr^{3+}:O^{2-}} + 15{,}350 - 7.9898T$

results, optimization of the parameter $^0L^{Corundum}_{Cr^{3+},Fe^{3+}:Va:O^{2-}}$ was undertaken. The optimized phase diagram of the Fe_3O_4–Cr_2O_3 system is illustrated in Fig. 7. And at high temperature, there is only one liquid phase and no miscibility gap.

The phase diagram of the Fe_3O_4–CaO system, calculated using the thermodynamic parameters provided by Selleby and Sundman [17] at oxygen partial pressure of 0.15 Pa, is depicted in Fig. 8. The experimentally measured solid solubility of CaO in Fe_3O_4 is 2.9 wt.%, aligning with the calculated results. Additionally, the calculated eutectic reaction temperature for the Liquid → $Ca_2Fe_2O_5$ + Fe_3O_4 is 1475 K, matching the temperature measured by DSC in this work. However, there is a slight discrepancy in the liquid composition. The calculated value is 77.6 wt.% Fe_3O_4, whereas the experimentally measured composition is 81.9 wt.% Fe_3O_4. The Fe_3O_4–CaO binary system is actually a projection of the FeO–Fe_2O_3–CaO ternary system along the Fe_3O_4–CaO direction. In the actual process, the starting position of Fe_3O_4 may deviate slightly from the calculated position, because in the FeO–Fe_2O_3–CaO ternary system, the position of Fe_3O_4 is a region rather than a point at high temperature. Therefore, this set of thermodynamic parameters has been selected for extrapolating the isothermal section of the Fe_3O_4–Cr_2O_3–CaO system at 1473 K.

The calculated phase diagram of the CaO–Cr_2O_3 system under oxygen partial pressure of 0.15 Pa is illustrated in Fig. 9. Within this system, only $CaCr_2O_4$ is taken into consideration for optimization. The low-temperature β form of $CaCr_2O_4$ exhibits a spinel structure, whereas the high-temperature α form parallels the structure of $SrCr_2O_4$.

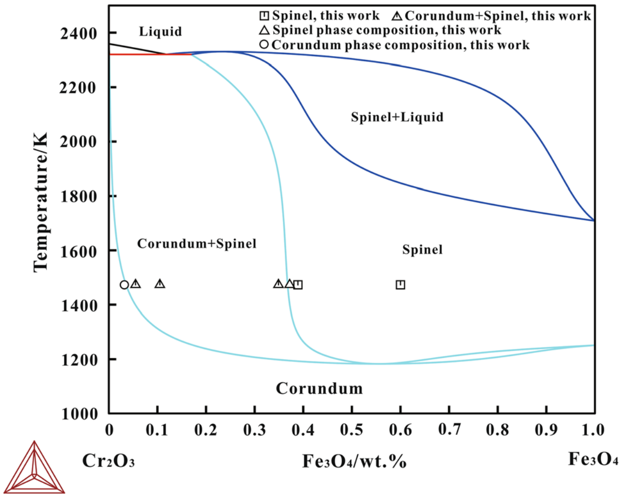

Fig. 7 Calculated phase diagram of Fe_3O_4–Cr_2O_3 system under oxygen partial pressure of 0.15 Pa with experimental data

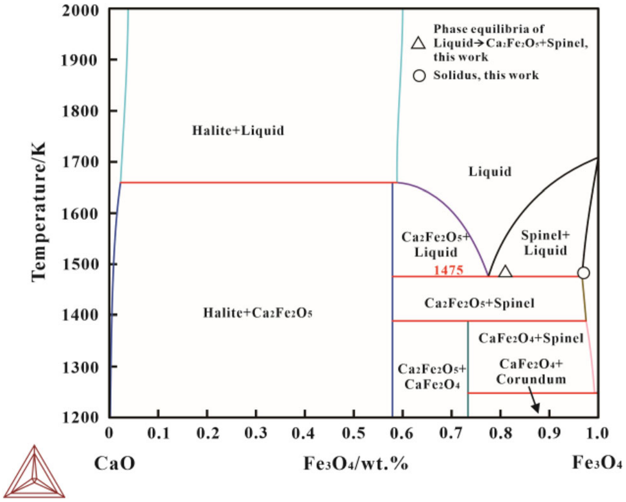

Fig. 8 Calculated phase diagram of Fe_3O_4–CaO system under oxygen partial pressure of 0.15 Pa with experimental data

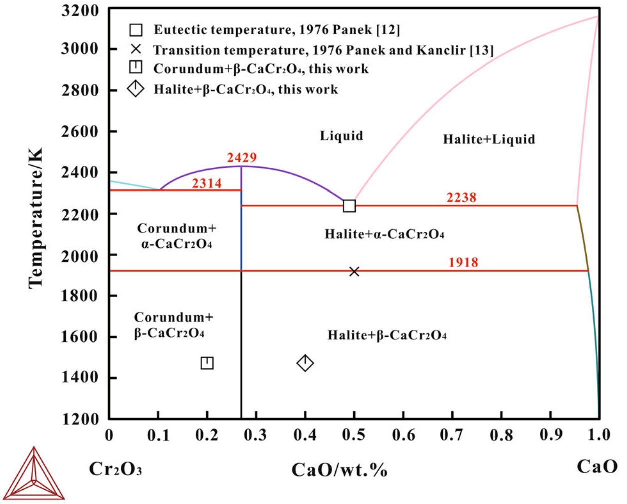

Fig. 9 Calculated phase diagram of CaO–Cr_2O_3 system under oxygen partial pressure of 0.15 Pa with experimental data [12, 13]

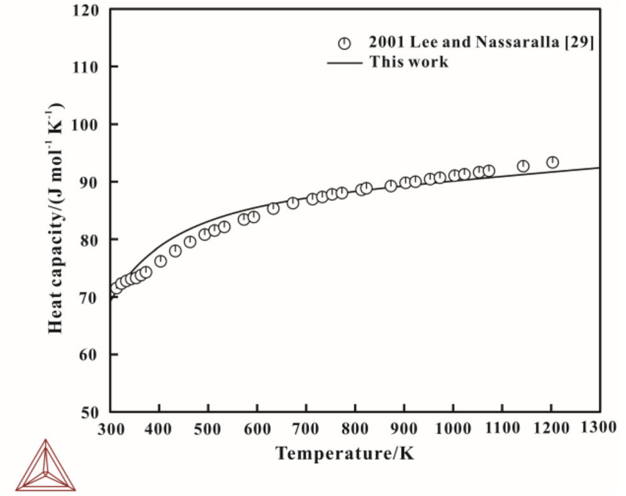

Fig. 10 Calculated heat capacity of β-$CaCr_2O_4$ with the experimental data [29]

The transition temperature between α-$CaCr_2O_4$ and β-$CaCr_2O_4$ is calculated to be 1918 K, aligning with the experimental findings of Panek and Kanclir [13]. Additionally, $CaCr_2O_4$ also possesses a metastable δ form. The CALPHAD method focuses on determining the variation of Gibbs free energy in relation to the system's composition at each temperature, thereby identifying the phase of equilibrium coexistence when the system's total Gibbs energy is minimized. Since a metastable phase is not thermodynamically stable and only temporarily stable due to thermodynamic energy barriers or dynamic factors, it typically has a higher Gibbs energy compared to the stable phase. Therefore, the δ-$CaCr_2O_4$ form is not included in the optimization process. The calculated heat capacity of β-$CaCr_2O_4$, compared with experimental data [29], is shown in Fig. 10. The heat capacity of $CaCr_2O_4$ was estimated using the Neumann–Kopp rule based on heat capacity data of CaO and Cr_2O_3, yielding results broadly consistent with the experimental data reported by Lee and Nassaralla [29]. The calculated eutectic temperature for Liquid → CaO + $CaCr_2O_4$ is 2238 K, in agreement with the experiments conducted by Panek [12]. Ol'shanskii et al. [14] reported a eutectic reaction involving Liquid → Cr_2O_3 + $CaCr_2O_4$. The eutectic temperature for this reaction is higher than that of Liquid → CaO + $CaCr_2O_4$, though it has not been precisely measured. In this study, a eutectic temperature of 2314 K is adopted. The maximum solid solubility of Cr_2O_3 in the CaO phase is calculated to be 4.7 wt.%.

5 Discussion

The ternary phase diagram can be inferred from the thermodynamic data of binary systems. This is accomplished by multiplying the thermodynamic parameters of the binary systems by weight factors and summing them up to represent the thermodynamic properties of the ternary system. By integrating the phase diagrams of the three binary systems of Fe_3O_4–Cr_2O_3, Fe_3O_4–CaO and CaO–Cr_2O_3, the ternary phase diagram of the Fe_3O_4–Cr_2O_3–CaO system can be extrapolated. However, it is important to note that such direct extrapolation does not account for the solid solubility of compounds or the potential formation of new ternary compounds. Therefore, some discrepancies may exist between the extrapolated phase diagram and the actual experimental observations. The extrapolated isothermal section of the Fe_3O_4–Cr_2O_3–CaO system at 1473 K under oxygen partial pressure of 0.15 Pa is presented in Fig. 11.

As depicted in Fig. 11, the Fe_3O_4–Cr_2O_3–CaO system at 1473 K exhibits twelve major types of phase equilibrium relationships. These include three-phase equilibrium among β-$CaCr_2O_4$, $Ca_2Fe_2O_5$, and halite, three-phase equilibrium involving the liquid phase, $Ca_2Fe_2O_5$, and spinel, three-phase equilibrium among β-$CaCr_2O_4$, $Ca_2Fe_2O_5$, and spinel, three-phase equilibrium among β-$CaCr_2O_4$, corundum, and spinel, two-phase equilibrium between the liquid phase and $Ca_2Fe_2O_5$, two-phase equilibrium between the liquid phase and spinel, two-phase equilibrium between $Ca_2Fe_2O_5$ and spinel, two-phase equilibrium between β-$CaCr_2O_4$ and spinel, two-phase equilibrium between corundum and spinel, two-phase equilibrium between β-$CaCr_2O_4$ and corundum, a single spinel phase, and a single liquid phase. Interestingly, despite the absence of a liquid phase in the corresponding binary systems at 1473 K, the isothermal section extrapolated from thermodynamic parameters of the binary systems reveals a narrow liquid phase region. This observation underscores the complexities and interactions within the ternary system that may not be immediately apparent from the binary phase diagrams alone.

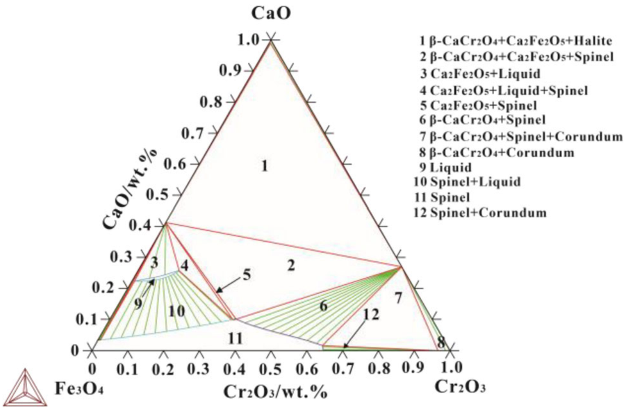

Fig. 11 Extrapolated isothermal section of Fe_3O_4–Cr_2O_3–CaO system at 1473 K under oxygen partial pressure of 0.15 Pa

In the Fe_3O_4–Cr_2O_3–CaO system at 1473 K, Cr^{3+} and Ca^{2+} ions have the potential to substitute Fe^{3+} and Fe^{2+} ions in Fe_3O_4, respectively, leading to the formation of a (Fe, Ca)(Fe, Cr)$_2$O$_4$ solid solution. This substitution results in a spinel single-phase region within the isothermal section of the system. However, the solid solubility limits of CaO and Cr_2O_3 in Fe_3O_4 are 2.9 and 62.8 wt.%, respectively, suggesting that the spinel phase is predominantly chromite ($FeCr_2O_4$). Identifying the phase region of chromite is critical for the recovery of valuable chromium from stainless steel pickling sludge. β-$CaCr_2O_4$ and $CaFe_2O_4$ share similar structural characteristics, and both are part of the orthorhombic system with the space group Pbnm. Consequently, a solid solution forms between β-$CaCr_2O_4$ and $CaFe_2O_4$. Amberúz et al. [30] have previously studied the phase equilibrium of the $CaCr_2O_4$–$CaFe_2O_4$ system and reported the formation of a Ca(Cr, Fe)$_2$O$_4$ solid solution. However, the extrapolation results do not account for the solid solubility of the third component in the binary compound. Thus, future work should focus on exploring the Ca(Cr, Fe)$_2$O$_4$ solid solution and completing the isothermal section of the system at 1473 K under oxygen partial pressure of 0.15 Pa, to provide a more comprehensive understanding of the system's phase behavior.

6 Conclusions

1. The solid solubility of Cr_2O_3 in Fe_3O_4 at 1473 K was clarified. Additionally, the eutectic reaction involving Liquid → $Ca_2Fe_2O_5$ + Fe_3O_4 was investigated. Under the specified oxygen partial pressure at 1473 K, the CaO–Cr_2O_3 system was found to form β-$CaCr_2O_4$.
2. Utilizing the ionic two-sublattice model to describe the liquid phase in the CaO–Cr_2O_3 binary system, a self-consistent set of thermodynamic parameters for this system was established. This was achieved using reliable experimental data from both the literature and the current study. Furthermore, the solid solubility of Fe_3O_4 in Cr_2O_3 at 1473 K was optimized based on experimental findings from this work.
3. The calculated isothermal section of the Fe_3O_4–Cr_2O_3–CaO system at 1473 K under oxygen partial pressure of 0.15 Pa was determined using the thermodynamic parameters of the binary systems. This enabled the

identification of the phase region of chromite at 1473 K, providing a theoretical foundation for the recycling of valuable metal chromium from stainless steel pickling sludge.

Supplementary Information The online version contains supplementary material available at https://doi.org/10.1007/s42243-024-01225-2.

Acknowledgements The financial supports on the Project 52274306 from the National Natural Science Foundation of China are gratefully acknowledged.

Declarations

Conflict of interest Pei-yuan Ni is a youth editorial board member for the *Journal of Iron and Steel Research International* and was not involved in the editorial review or the decision to publish this article. The authors declare that they have no known competing financial interests or personal relationships that could have appeared to influence the work reported in this paper.

References

[1] L.F. Li, P. Caenen, M. Daerden, D. Vaes, G. Meers, C. Dhondt, J.P. Celis, Corros. Sci. 47 (2005) 1307–1324.

[2] L.F. Li, M. Daerden, P. Caenen, J.P. Celis, J. Electrochem. Soc. 153 (2006) B145.

[3] A. Singhal, V.K. Tewari, S. Prakash, Build. Environ. 43 (2008) 1010–1015.

[4] M.T. Wu, Y.L. Li, Q. Guo, D.W. Shao, M.M. He, T. Qi, J. Clean. Prod. 240 (2019) 118187.

[5] P. Ma, B. Lindblom, B. Björkman, Scand. J. Metall. 34 (2005) 31–40.

[6] L. Kaufman, H. Bernstein, Computer calculation of phase diagrams, Academic Press, New York, USA, 1970.

[7] A. Muan, S. Omiya, J. Am. Ceram. Soc. 43 (1960) 204–209.

[8] P.V. Riboud, A. Muan, Trans. Met. Soc. AIME 230 (1964) 88–90.

[9] B. Phillips, A. Muan, J. Am. Ceram. Soc. 41 (1958) 445–454.

[10] W.C. Allen, R.B. Snow, J. Am. Ceram. Soc. 38 (1955) 264–272.

[11] A. Kaiser, B. Sommer, E. Woermann, J. Am. Ceram. Soc. 75 (1992) 1463–1471.

[12] Z. Panek, Silikaty 20 (1976) 1–12.

[13] Z. Panek, E. Kanclir, Silikaty 20 (1976) 113–121.

[14] Y.I. Ol'shanskii, A.I. Tsvetkov, V.K. Shlepov, Dokl. Akad. Nauk SSSR 96 (1954) 1007–1009.

[15] J.R. Taylor, A.T. Dinsdale, Z. Metallkd. 84 (1993) 335–345.

[16] L. Kjellqvist, M. Selleby, B. Sundman, Calphad 32 (2008) 577–592.

[17] M. Selleby, B. Sundman, Calphad 20 (1996) 381–392.

[18] S. Degterov, A.D. Pelton, J. Phase Equilibria 17 (1996) 476–487.

[19] M. Hillert, B. Jansson, B. Sundman, J. ågren, Metall. Trans. A 16 (1985) 261–266.

[20] B. Sundman, Calphad 15 (1991) 109–119.

[21] N. Saunders, A.P. Miodownik, CALPHAD (calculation of phase diagrams): a comprehensive guide, Pergamon, Oxford, UK, 1998.

[22] B. Sundman, B. Jansson, J.O. Andersson, Calphad 9 (1985) 153–190.

[23] B. Sundman, J. Phase Equilibria. 12 (1991) 127–140.

[24] M. Hillert, B. Jansson, B. Sundman, Int. J. Mater. Res. 79 (1988) 81–87.

[25] P.M. Hill, H.S. Peiser, J.R. Rait, Acta Crystallogr. 9 (1956) 981–986.

[26] F.P. Glasser, L.S. Dent Glasser, Inorg. Chem. 1 (1962) 428–429.

[27] S. Toth, B. Lake, S.A.J. Kimber, O. Pieper, M. Reehuis, A.T.M.N. Islam, O. Zaharko, C. Ritter, A.H. Hill, H. Ryll, K. Kiefer, D.N. Argyriou, A.J. Williams, Phys. Rev. B 84 (2011) 054452.

[28] S.E. Dutton, C.L. Broholm, R.J. Cava, J. Solid State Chem. 183 (2010) 1798–1804.

[29] Y.M. Lee, C.L. Nassaralla, Thermochim. Acta 371 (2001) 1–5.

[30] V. Ambrúz, J. Havlica, Z. Pánek, Silikaty 25 (1981) 15–20.